International Journal of Mechanical, Industrial and Aerospace Sciences
ISSN: 2517-9950
Vol:5, No:3, 2011

CFD Predictions of Dense Slurry Flow in Centrifugal Pump Casings

Krishnan V. Pagalthivarthi, Pankaj K. Gupta, Vipin Tyagi, M. R. Ravi

***Abstract*—**Dense slurry flow through centrifugal pump casing has been modeled using the Eulerian-Eulerian approach with Eulerian multiphase model in FLUENT 6.1®. First order upwinding is considered for the discretization of momentum, k and ε terms. SIMPLE algorithm has been applied for dealing with pressure-velocity coupling. A mixture property based k-ε turbulence model has been used for modeling turbulence. Results are validated first against mesh independence and experiments for a particular set of operational and geometric conditions. Parametric analysis is then performed to determine the effect on important physical quantities viz. solid velocities, solid concentration and solid stresses near the wall with various operational geometric conditions of the pump.

***Keywords*—**Centrifugal pump casing, Dense slurry, Solids concentration, Wall shear stress, Pump geometric parameters.

I. Introduction

CENTRIFUGAL pumps are widely used in transporting solid liquid slurries [1] from one point to another. They have wide applications in mining industry, chemical industry, metallurgical operations, coal industry and so on. In typical slurries, solid particles have a range of diameters and concentration depending on type of slurry for a particular application. The presence of solid particles affects the hydrodynamic and erosion performance of the pump. Performance reduction of the pump [2] and erosion damage of the wetted components [3] are two important and frequently faced problems when pumping solid-liquid mixtures.

The important pump wetted components that undergo severe erosion effects are the liners, the impeller and the pump casing. The pump casing is the heaviest component among the three wearing parts and its design is also very complex. Hence it is the costliest wearing component [3] of the pump.

In abrasive slurry applications, hard cast iron alloys (usually chromium-nickel) are used for the wetted components. Due to the difficulty in repairing such hard alloy cast iron materials, a local damaged area could render an otherwise serviceable component to be rejected. This leads to frequent replacement of spare parts. Each time a part is to be replaced, a complete shutdown of the pipeline operation is also necessitated. Therefore, from the viewpoints of hydrodynamic performance and useful life of pump components, flow field and erosion prediction in centrifugal pumps has attracted considerable interest and concern over the years.

Erosion wear is a complex surface (wall) phenomenon. It depends on the particulate velocity and concentration distribution along the wall surface. Other factors that influence wear performance include the particle size, abrasivity, material properties of the pump component and particles, flow rate [5], [6], pump speed [7] and so forth. The first step in erosion wear prediction [5]-[10] is the computation of the two-phase (solid-liquid) flow field within the component. Once the flow field is determined, the local concentration and velocity are correlated *via* the wear models [7]-[10] to predict wear rates.

The pump operates at a specific rotational speed, head and flow rate. There is also possibility of marginal variations in geometries of pump components. For example, casing geometry may be changed by varying impeller diameter, curvature of the tongue region or casing width within certain limits. For obtaining an optimally wearing pump, suitable changes in operational and geometric conditions of the pump can be effective. This necessitates computation of two-phase flow and is a vital step towards determining the local flow conditions near the wear surface.

Ideally, it would be best to model the entire pump (including all wetted components) as one flow system. However, this approach will prove extremely expensive and hence unsuitable as a design tool. A component-wise analysis is much more economical. A component-by-component approach serves readily the specific needs of a design engineer [10] and is also computationally efficient. Thus, this approach has been used in the present study to compute flow field of dense slurry in centrifugal pump casing by applying suitable boundary conditions.

Two dimensional models of the pump casings have been developed in the past [9], [11], [12]. These studies [9], [11], [12] included an inviscid approach in modeling slurry flow and had some crucial limitations viz., neglecting the viscous terms for particles greater than 1mm diameter, the procedure did not converge reliably. The models in these studies [9], [11-12] allowed some mass loss of the carrier phase flow through the casing wall. Neglect of pressure and gravity

K. V. Pagalthivarthi is with GIW Industries Inc., Wrightsboro Road, Georgia, GA – 30813, USA.
P. K. Gupta is with Mechanical Engineering Department, Raghu Engineering College, Visakhapatnam, AP – 531162, INDIA (Corresponding author; phone: +91-8922-248001; Fax: +91-8922-248011; E-mail: pankajkgupta@gmail.com).
V. Tyagi is with SHELL Technology India, Bangalore, INDIA.
M. R. Ravi is with Mechanical Engineering Department, Indian Institute of Technology Delhi, New Delhi – 110016, INDIA.

terms in force balance on the particles also limited the analysis to fine particles which follow the carrier fluid closely. Another drawback of the inviscid solution was that it could not predict reverse flow and separation. In a typical slurry pump, which has wide passages compared to a water pump, these effects can become quite important, especially for off-design conditions. These limitations were addressed in [13] using a quasi-3D model. The main contribution of the study [13] was the prediction of main stream and secondary flows at any arbitrary cross-section of the pump casing.

In another study [14], 2D Reynolds Averaged Navier Stokes (RANS) equations have been solved using Galerkin finite element method (GFEM) with four noded quadrilateral elements. The study [14] employs mixing length turbulence model for viscous predictions of the solid-liquid mixture inside the pump casing. The solids velocity field [14] when compared with the experimentally obtained instantaneous velocities using Particle Image Velocimetry (PIV) results [15] showed reasonable agreement within the scope of the modeling assumptions. Various other studies [16, 17] have addressed the influence of flow and geometry parameters on the velocity and pressure distribution in centrifugal pump casing using CFD. However, the analysis is restricted to single phase flow only.

The objective of the present study is therefore to numerically investigate and gain physical insight of the flow field of dense slurry in centrifugal pump casings subject to various operational and geometric conditions. The mid-plane of the slurry pump normal to the pump axis is considered for the analysis as shown in Fig. 1. The flow is assumed to be two-dimensional, incompressible and steady in the mean.

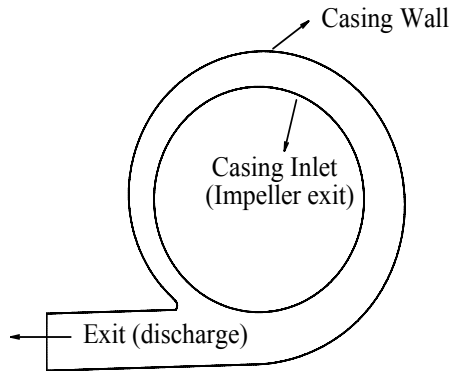

Fig. 1. Physical domain of the 2D slurry pump casing normal to the pump axis with various flow boundaries.

The dense slurry flow has been modeled using the continuum mechanical or Eulerian-Eulerian approach in FLUENT 6.1®. This approach is computationally viable choice [18]-[22] in preference to the Lagrangian particle tracking method. In Eulerian-based model, each phase is described as a continuum occupying the same region of space exchanging mass, momentum and energy with each other.

The numerical formulation is based on the finite volume method as implemented in FLUENT 6.1®. SIMPLE algorithm has been applied for dealing with pressure-velocity coupling. Mixing length model has been used widely by past researchers for turbulent predictions of slurry flow owing to its simplicity. The present study however employs mixture based $k-\varepsilon$ turbulence model in FLUENT 6.1®, which is more suited for complex geometry flows. First order upwinding is considered for the discretization of momentum, k and ε terms.

II. Mathematical and Numerical Formulation

A. Mathematical Formulation

In the continuum-mechanical or Eulerian approach, the volume-averaged, steady continuity and momentum equations are presented for each phase. Let $\vec{u}_S$, $\vec{u}_L$; C_S, C_L and ρ_S, ρ_L denote the velocity, volumetric concentration and density of the solid and the carrier phase respectively. Sum of the solid and liquid concentrations is equal to unity. With these definitions, using intrinsic average quantities, the steady continuity equations for solid and liquid phases are written as

$$\nabla.\left(C_k \rho_k \vec{v}_k\right) = 0, \tag{1}$$

where k is the representative index for solid and liquid phases. Similarly, the steady momentum equation for solid and liquid phases is

$$\nabla.\left(C_k \rho_k \vec{v}_k \vec{v}_k\right) = -C_k \nabla p + \nabla.\left(C_k \underline{\tau}_k\right) + C_k \rho_k \vec{g} + \vec{R} + C_k \rho_k \left(\vec{F}_k + \vec{F}_{lift,k} + \vec{F}_{vm,k}\right) \tag{2}$$

where p is the pressure, $\underline{\tau}_k$ is the stress tensor, $\vec{g}$ is the acceleration due to gravity and $\vec{R}$ is the interaction force between the phases. The pressure p is assumed to be same for all the phases. The pressure at the interface between the phases is assumed to be the average pressure [23].

In the last term (Right Hand Side) of Eq. (2), $\vec{F}_k$ is the body force, $\vec{F}_{lift,k}$ is a lift force and $\vec{F}_{vm,k}$ is the virtual mass force per unit mass of the phase k. The lift force acting on solid phase S in a carrier phase L is computed as

$$\vec{F}_{lift,S} = -0.5 \rho_L \alpha_S \left(\vec{v}_L - \vec{v}_S\right) \times \left(\nabla \times \vec{v}_L\right). \tag{3}$$

The lift force will be added to the right side of the momentum equations of solid and carrier phases with an opposite sign in the latter, i.e. $\vec{F}_{lift,L} = -\vec{F}_{lift,S}$.

Virtual mass effect occurs when the solid phase S accelerates relative to the carrier phase L. The inertia of the carrier phase mass encountered by the accelerating particles exerts a virtual mass force on the particles. This is given as

$$\vec{F}_{vm} = 0.5 \alpha_S \rho_L \left(\frac{d_L \vec{v}_L - d_S \vec{v}_S}{dt}\right), \tag{4}$$

where $\frac{d_k}{dt}$ denotes the phase material derivative of the form of $\frac{d_k(\phi)}{dt} = \frac{d(\phi)}{dt} + \left(\vec{v}_k.\nabla\right)\phi$. It should be noted that $\vec{F}_{vm,L} = -\vec{F}_{vm,S}$.

The interactive force predominantly consists of interactive drag between the solid phase (*S*) and the carrier phase (*L*). The interaction force $\vec{R}_{SL}$ (*SL* indicates solid-liquid interaction) is subjected to the condition that $\vec{R}_{SL} = -\vec{R}_{LS}$. This interaction force between solid and liquid phases can be further simplified as $\vec{R}_{SL} = K_{SL}\left(\vec{v}_S - \vec{v}_L\right)$ where K_{SL} is the interphase momentum exchange coefficient. The fluid-solid exchange coefficient $\left(K_{SL}\right)$ from the model of [24] available in FLUENT 6.1® is of the form

$$K_{SL} = \frac{3}{4} C_D \frac{\alpha_S \alpha_L \rho_L \left|\vec{v}_S - \vec{v}_L\right|}{d_S} \alpha_L^{-2.65} \tag{5}$$

$$\text{with } C_D = \frac{24}{\alpha_L Re_S}\left[1 + 0.5\left(\alpha_L Re_S\right)^{0.687}\right], \tag{6}$$

where

$$Re_S = \frac{\rho_L d_S \left|\vec{v}_S - \vec{v}_L\right|}{\mu_L}. \tag{7}$$

In FLUENT implementation, the viscosities are obtained by making an analogy between the random motion arising from the particle-particle collisions and the thermal motion of molecules in a gas according to the kinetic theory of gases. The solid stress tensor contains shear viscosity, μ_{St}, arising from the particle momentum exchange due to translation and collision. The shear viscosity of the solid is obtained as the summation of collisional and kinetic parts as per the following expressions

$$\mu_S = \mu_{S,col} + \mu_{S,kin} \tag{8}$$

$$\mu_{S,col} = \frac{4}{5} C_S \rho_S d_S g_0 \left(1 + e_{SS}\right)\left(\frac{\Theta_S}{\pi}\right)^{1/2} \tag{9}$$

and

$$\mu_{S,kin} = \frac{10 \rho_S d_S \sqrt{\Theta_S \pi}}{96 C_S \left(1 + e_{SS}\right) g_0}\left[1 + \frac{4}{5} g_0 C_S \left(1 + e_{SS}\right)\right]^2 \tag{10}$$

For granular flows, a solids pressure is calculated independently and is used for the pressure gradient term, ∇p_S in the solid phase momentum equation. A Maxwellian velocity distribution is used for the particles; a granular temperature is hence introduced into the model and appears in the expression for the solids pressure and viscosities. The solids pressure is composed of a kinetic term and a second term due to particle collisions, so that

$$p_S = C_S \rho_S \Theta_S + 2\rho_S \left(1 + e_{SS}\right) C_S^2 g_0 \Theta_S \tag{11}$$

where e_{ss} is the coefficient of restitution for particle collisions, g_0, is the radial distribution function, and Θ_s is the granular temperature. The granular temperature $\left(\Theta_s\right)$ is proportional to the kinetic energy of the fluctuating particle motion. The function g_0 is a distribution function that governs the transition from "compressible" condition with $\alpha < \alpha_{S,\max}$, where the spacing between the solid particles can continue to decrease, to the "incompressible" condition with $\alpha = \alpha_{S,\max}$, where no further decrease in the spacing can take place. The radial distribution function is defined as

$$g_0 = \left[1 - \left(\frac{\alpha_S}{\alpha_{S,\max}}\right)^{\frac{1}{3}}\right]^{-1}. \tag{12}$$

Standard wall functions are applied for liquid and solid phase along the casing wall in FLUENT implementation as

$$U^* = \frac{1}{\kappa}\ln\left(Ey^*\right)$$

$$y^* = \frac{\rho C_\mu^{1/4} k_p^{1/2} y_p}{\mu} \tag{13}$$

where k_P is the turbulence kinetic energy at point *P*, and y_P is the distance from point *P* to the wall. It should be noted that law of the wall in FLUENT 6.1® are based on y^* rather than y^+. At the inlet, boundary conditions are prescribed as $\vec{u}_S = \vec{u}_L, i.e,$

$$u_\theta = \frac{gH}{\eta u_S};\ u_r = \frac{Q}{2\pi Rb},\ C_S = C_{average}. \tag{14}$$

These are specified using the "velocity inlet" type of boundary condition in FLUENT 6.1®. At the exit, zero gradient boundary condition is specified using the "outflow" type of boundary condition as

$$\frac{\partial p}{\partial x} = 0;\ \frac{\partial u_{S,L}}{\partial x} = 0;\ \frac{\partial v_{S,L}}{\partial x} = 0. \tag{15}$$

In the present work, non-orthogonal grids are used. The numerical formulation for application of SIMPLE or alike algorithms in collocated grids for the solution of equations is slightly different than that for staggered grids.

B. Turbulence

FLUENT 6.1® offers three different turbulence models. Most simple and general amongst them is the mixture turbulence model. It uses mixture velocities and mixture properties, and is assumed to sufficiently capture the important features of turbulent flow. The present study primarily concerns itself with the mixture $k-\varepsilon$ turbulence model which is widely used in industrial research work. The governing equations for mixture $k-\varepsilon$ turbulence model are as follows:

$$\nabla.\left(\rho_m \vec{v}_m k\right) = \nabla.\left(\frac{\mu_{t,m}}{\sigma_k}\nabla k\right) + G_{k,m} - \rho_m \varepsilon \tag{16}$$

and

$$\nabla.\left(\rho_m \vec{v}_m \varepsilon\right) = \nabla.\left(\frac{\mu_{t,m}}{\sigma_\varepsilon}\nabla \varepsilon\right) + \frac{\varepsilon}{k}\left(C_{1\varepsilon} G_{k,m} - C_{2\varepsilon}\rho_m \varepsilon\right). \tag{17}$$

The mixture density and velocity, ρ_m and $\vec{v}_m$, are computed respectively, as

$\rho_m = \alpha_S \rho_S + \alpha_L \rho_L$ and

$$\vec{v}_m = \frac{\alpha_S \rho_S \vec{v}_S + \alpha_L \rho_L \vec{v}_L}{\alpha_S \rho_S + \alpha_L \rho_L}. \tag{18}$$

The turbulent viscosity, $\mu_{t,m}$ is computed as $\mu_{t,m} = \rho_m C_\mu \frac{k^2}{\varepsilon}$, and the production of turbulence kinetic energy, $G_{k,m}$, is computed as

$$G_{k,m} = \mu_{t,m}\left(\nabla\vec{v}_m + \left(\nabla\vec{v}_m\right)^T\right):\nabla\vec{v}_m \quad (19)$$

The constants in the above equations are same as in the single phase standard $k-\varepsilon$ turbulence model, and $\sigma_k = 1$, $\sigma_\varepsilon = 1.3$, $C_{1\varepsilon} = 1.44$ and $C_{2\varepsilon} = 1.92$ are empirical constants.

The governing equations in FLUENT 6.1® are solved using the segregated solver. In segregated solver, equations are solved sequentially unlike the coupled solver where the equations are solved in a coupled manner. In the segregated solution method, each governing equation is linearized implicitly with respect to the dependent variable in that governing equation. This results in a system of linear equations with one equation for each cell in the domain.

SIMPLE algorithm has been used for pressure-velocity coupling. FLUENT 6.1® uses a multigrid scheme to accelerate the convergence of the solver by computing corrections on a series of coarse grid levels. The use of the multigrid scheme can greatly reduce the number of iterations and the CPU time required to obtain a converged solution.

A residual convergence of 10^{-6} has been obtained for the governing variables *viz.* continuity, *u* and *v* of solid and liquid phase, *k* and ε, and volume fraction. Initially under-relaxation parameters were kept low and gradually increased when the residual stabilized.

III. Validation

The predicted flow field is validated in two stages. Firstly, by mesh refinement studies, and secondly, by comparison with experimental and numerical data published in the literature.

A. Mesh Refinement Studies

The pump casing considered for presenting mesh refinement studies has diameter of 0.4074m and the flow parameters as: Head (H) of 12.2m; flow rate (Q) of 0.02 m^3/s; pump efficiency of 73% and pump speed of 710 RPM (Refer Casing No. 1 of Table 1). Note that the flow rate is 100% BEPQ (Best Efficiency Point flow rate).

Mesh characteristics in terms of the number of cells and their computational time are provided in the Table 2 for dense slurry flow modeling using Eulerian model in FLUENT 6.1®.

TABLE I PUMP CASING INPUT DATA FOR THREE GEOMETRIES AT A GIVEN RPM. NOTE THAT ONLY 100% BEPQ (BEST EFFICIENCY POINT FLOW RATE) IS SHOWN

Casing No.	Impeller diameter (m)	H (m)	Q (m^3/s)	η	RPM
1	0.4	12.2	.02	0.73	710
2	0.225	63.5	.0444	0.71	3400
3	0.395	74	0.088	0.75	1900
4	0.502	77.5	.17	0.82	1400

TABLE II COMPUTATION TIME FOR VARIOUS MESHES

Mesh	Number of Cells	Time in minutes
1	18440	120 min
2	30,000	300 min
3	40,500	720 min

The densest mesh with 40,500 cells is computationally six times more expensive than the coarsest mesh with 18,440 cells.

Mesh independence is verified by comparing the solutions of velocity vectors, solids velocity and concentration profiles at various cross-sections inside the pump casing for these meshes as shown in Fig. 2, 3 and 4, respectively. The profiles are shown along 12'o clock, 3'o clock, 6'o clock, 9'o clock and exit sections in the pump casing domain. The velocity vectors in Fig. 3 compare well and bear same magnitude for the three meshes. The maximum discrepancy (relative error) in the velocity profiles along various pump cross-sections amount to 3.3% (see Fig. 3) and in concentration profiles to 4% (see Fig. 4). Finally, the coarsest grid with 18,400 cells which is shown to bear the mesh independent nature is used for parametric studies and presentation of results. In these simulations a particle concentration C_S of 20%, density of 2650 kg/m^3 and a particle diameter of 100μm has been considered.

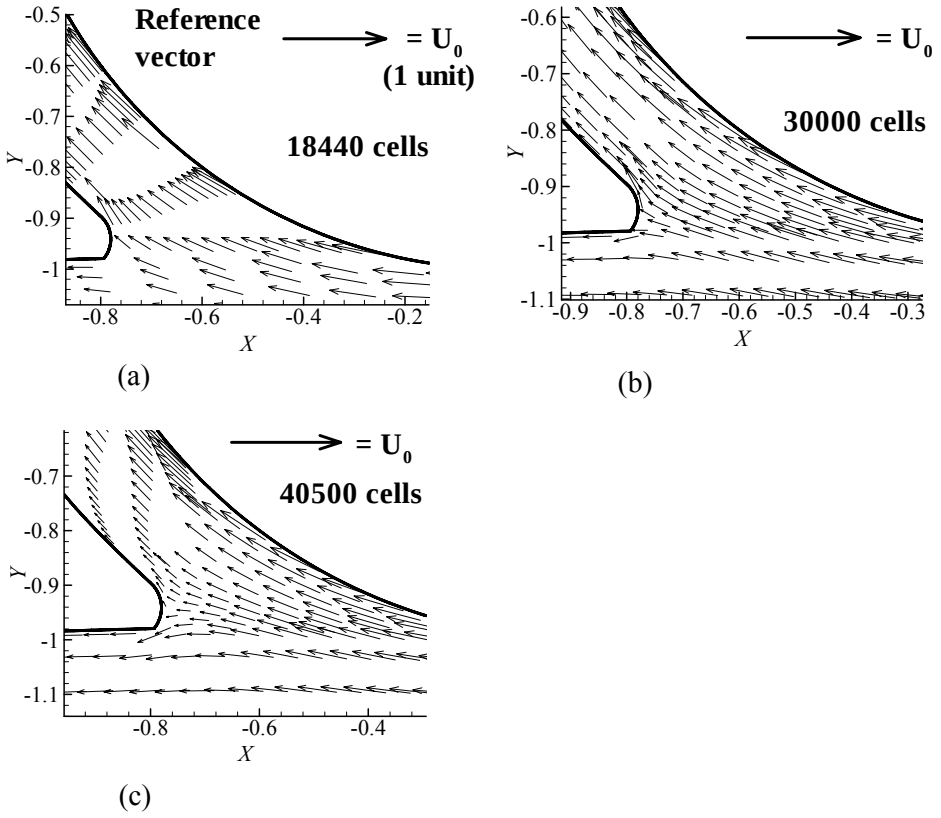

Fig. 2 Velocity vectors inside the pump casing in the tongue region for various meshes in Table 2. Note that the reference vector indicates the velocity of impeller tip (U_0).

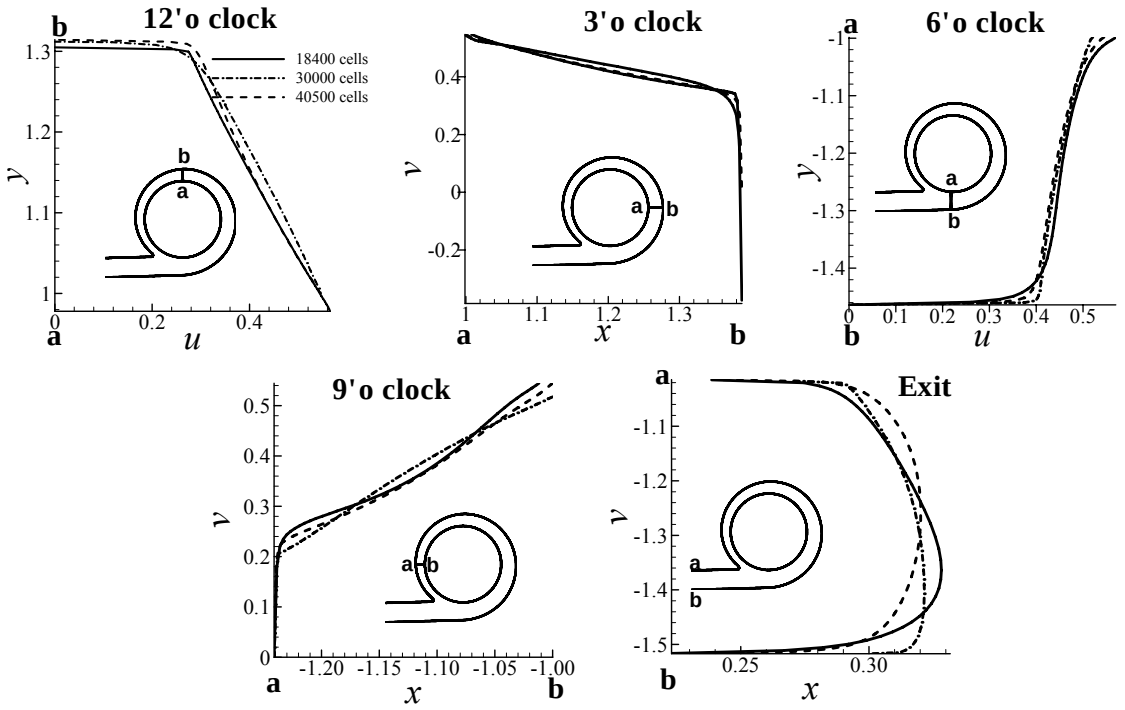

Fig. 3. Solid velocity profiles for various meshes in Table 2 shown along various pump cross-sections *viz.* 12'o clock, 3'o clock, 6'o clock, 9'o clock and exit.

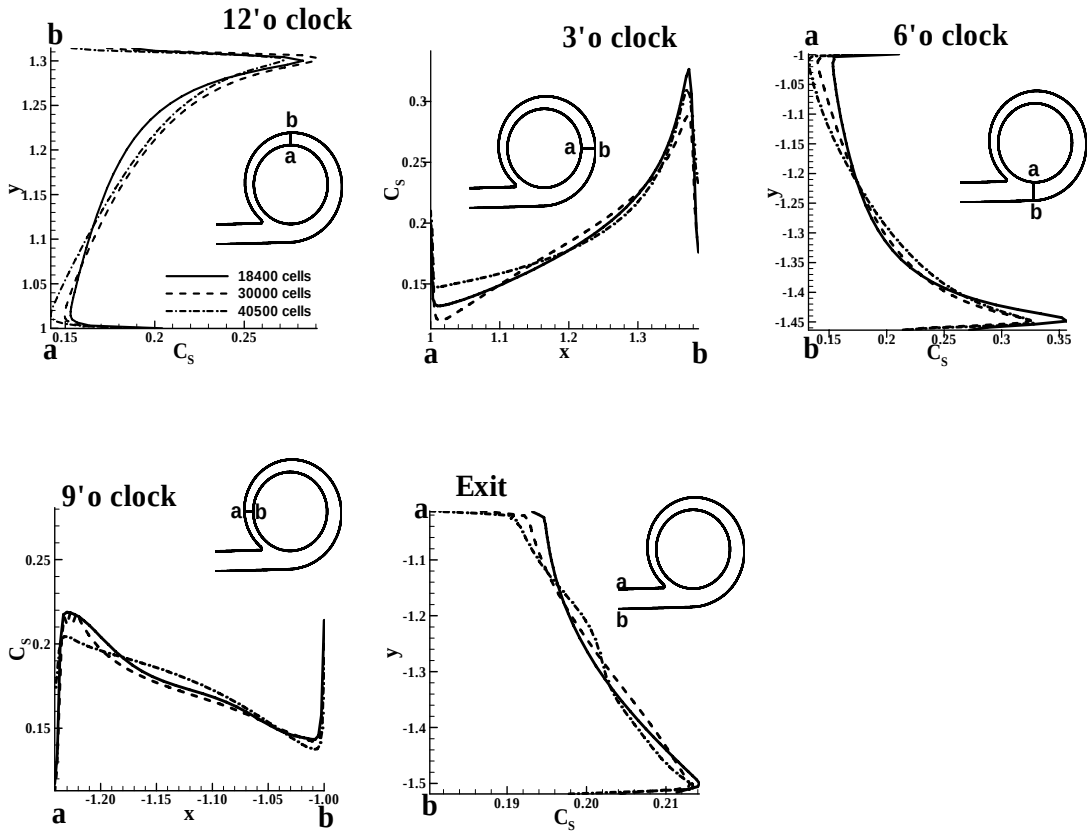

Fig. 4. Solid concentration profiles for various meshes in Table 2 shown along different pump cross-sections *viz.* 12'o clock, 3'o clock, 6'o clock, 9'o clock and exit.

A. Validation with Published Experimental and Numerical Results

Validation of present predictions is done by comparison with experimental data and numerical results published in the literature. First a comparison of particle concentration and velocity profiles along a channel cross-section has been made between present predictions and experimental data available in the literature [9]. Next, a comparison between present predictions and FEM based numerical solutions from [14] has been made for pump casing.

Fig. 5 shows the comparison between present predictions and experimental data of [9] for a channel flow problem. An average sized particle of 165μm diameter with a particle density of 2680 kg/m^3 is modeled in water as carrier phase having an inlet particle concentration of 8.41% by volume. The channel has its dimensions as 6m × 2m × 0.05m with an aspect ratio (length to height ratio) of 120. The average carrier phase velocity at the inlet of the channel is 1.66 m/s. In Fig. 5, velocities are normalized by average inlet velocity (1.66 m/s). We find a good comparison of velocities and concentration profiles across the channel height between present predictions from Eulerian model and experimental data from [9]. A maximum error of 6% is seen in the predictions with FLUENT 6.1® Eulerian multiphase model.

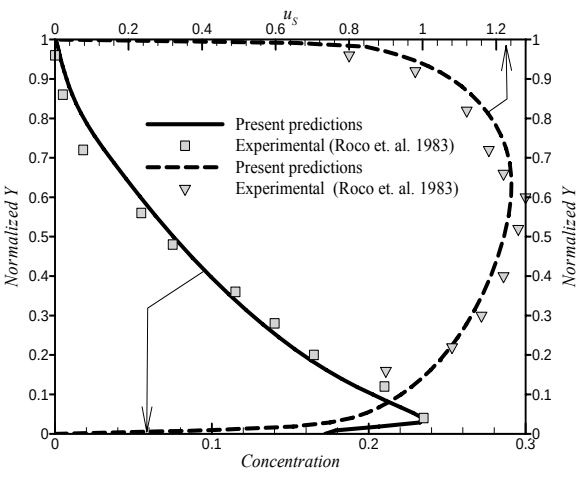

Fig. 5. Comparison of normalized velocity profile (right Y axis) and concentration profile (left Y axis) in a 2D channel with [9]. The channel height is shown normalized.

Next, we present the comparison of present predictions

with Finite Element Method (FEM) based predictions [14] for a centrifugal pump. The carrier phase and solid phase properties used in these simulations are given as: Flow rate (Q) = 170 US GPM (0.01 m^3/s), RPM =1000, H = 25 ft (7.62m), C_S (Average solid concentration) = 5%, liquid density (ρ) = 1690 kg/m^3, solid density (ρ_S) = 2650 kg/m^3.

In the FEM predictions, a mixing length model for turbulence has been employed; while in the present studies using FLUENT 6.1®, mixture properties based *k-ε* turbulence model has been employed. In Figs. 6-8, the profiles for the carrier phase velocity, solid velocity and solid concentration at various pump cross-sections respectively are compared with FEM based predictions from [14]. The maximum deviation between the two numerical solutions (present and FEM) is 12%. The usage of different eddy viscosity models can be one of the important reasons for this deviation between the two numerical solutions.

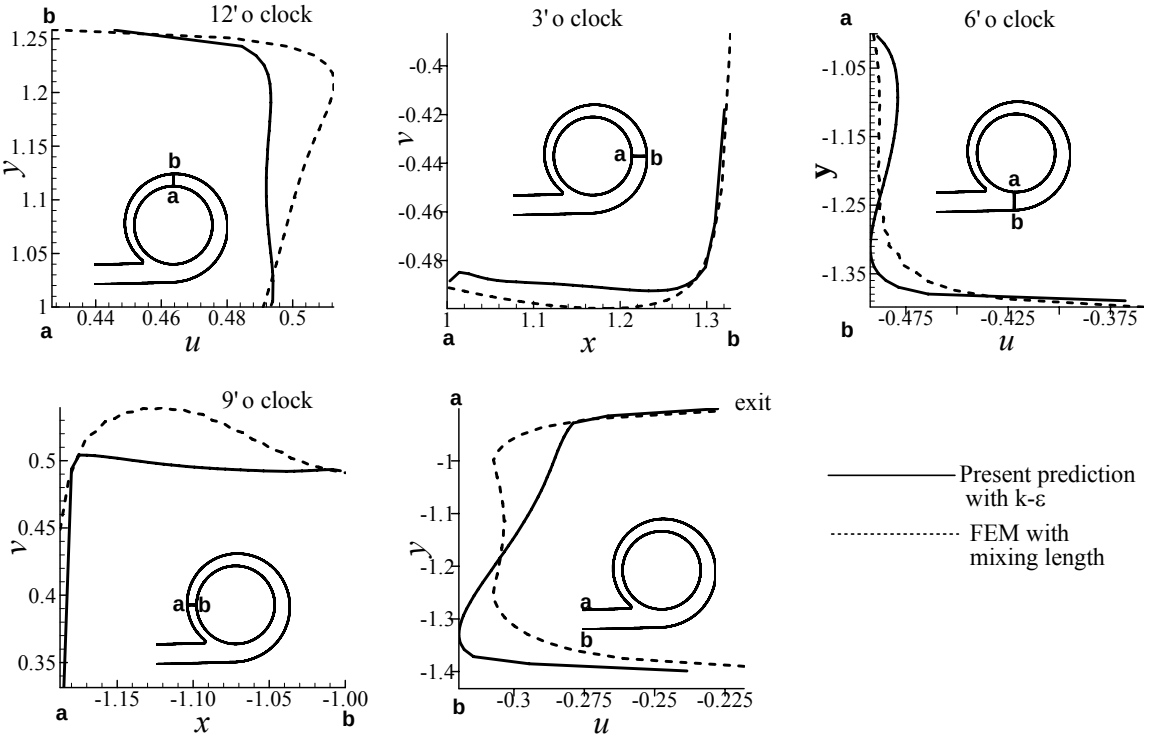

Fig. 6. Carrier phase velocity profiles from FLUENT 6.1® compared with FEM (Finite Element Method) results of [14] along various cross-sections *viz.* 12'o clock, 3'o clock, 6'o clock, 9'o clock and exit section.

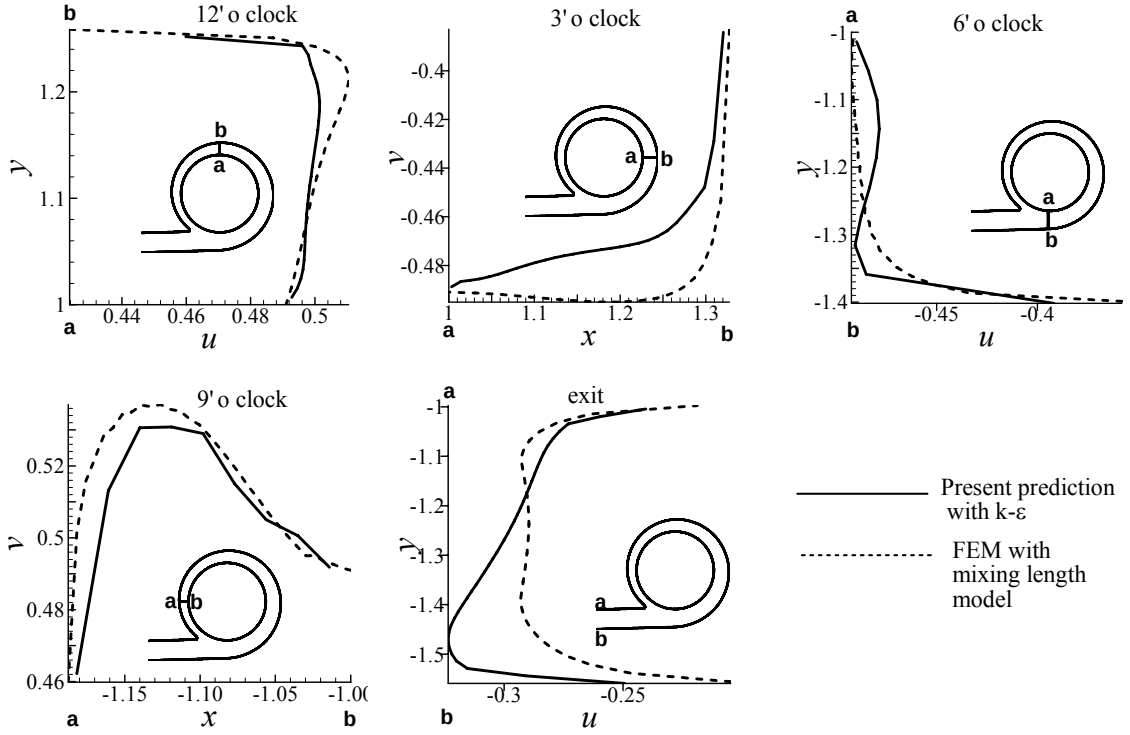

Fig. 7. Solid velocity profiles along various pump cross-sections *viz.* 12'o clock, 3'o clock, 6'o clock, 9'o clock and exit section inside the pump casing compared with numerical FEM based results of [14] for an inlet particle concentration of 5%.

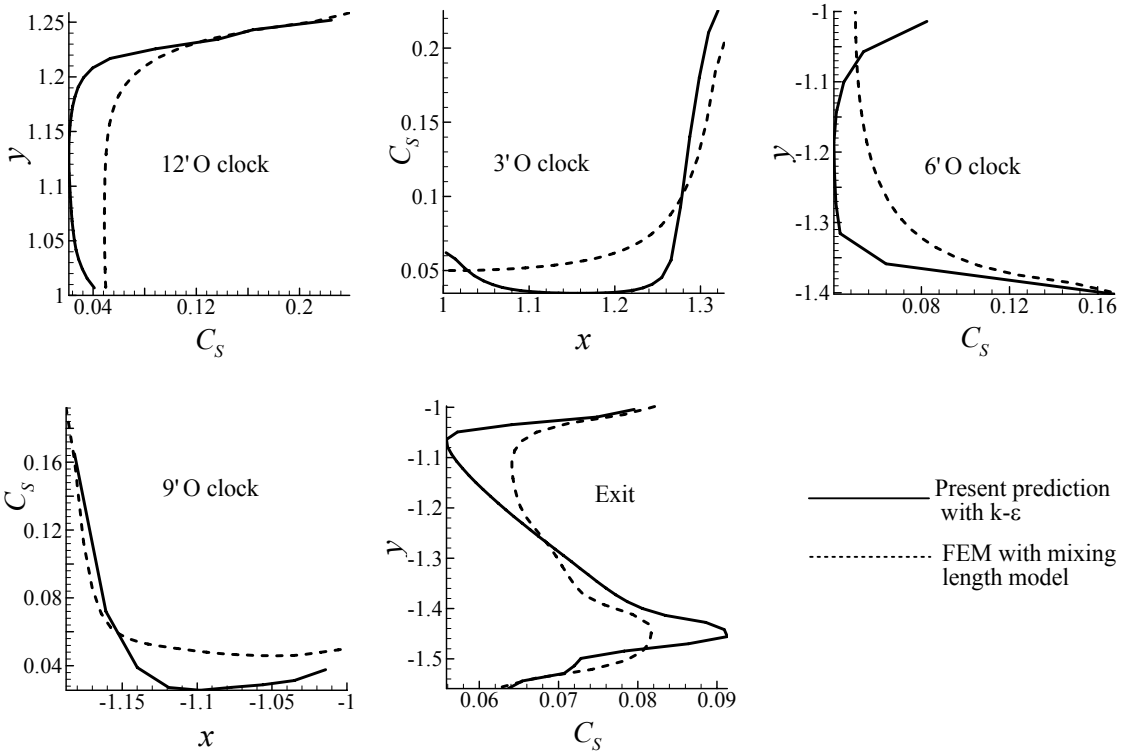

Fig. 8. Solid concentration profiles along various pump cross-sections *viz.* 12'o clock, 3'o clock, 6'o clock, 9'o clock and exit section inside the pump casing compared with numerical FEM results of [14].

IV. Results and Discussions

Detailed results for the pump casing are presented first while keeping the operational and geometric conditions same. Next the results of important physical quantities such as solids velocity, solids concentration and solid shear stresses along/near the wall are presented with geometrical and operational variations. These physical quantities are critical and a precursor to wear calculations.

The casing considered here is having an impeller diameter of 395 mm and a speed (RPM) of 1900 (Casing No.3 in Table 1) with water as the carrier phase and solid particle (diameter = 100 μm, ρ =2650 kg/m^3) as the dispersed phase. An average inlet particle concentration of 20% has been considered.

Fig. 9 shows the pressure distribution inside the pump casing. Pressure reaches its maximum near the tongue region of the pump casing. The values are indicated along the contour lines in the casing domain. Note that X and Y axis are non-dimensionalized by the radius of the impeller (here 0.1975 m) and pressure is non dimensionalized w.r.t. ρU_0^2 where U_0 is the impeller tip speed.

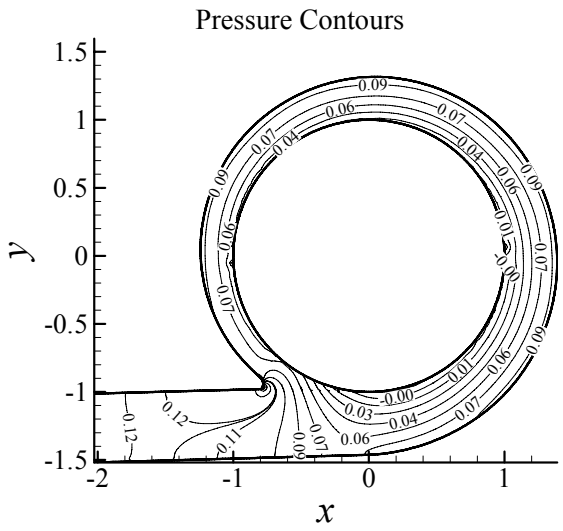

Fig. 9. Pressure distribution inside the 2D pump casing (Casing No. 3 in Table 1).

Fig. 10 shows the concentration contours inside the casing domain for an average particle concentration of 20% at the casing inlet. The concentration contours show a higher concentration near the wall which rises around the shell length and reaches highest in the belly region (0.33). Non uniform particle concentration near the wall as will be revealed in the discussion affects significantly the wear rate along the casing wall. Along the exit of the pump, the concentration varies between 0.16 and 0.23 as seen from the figure.

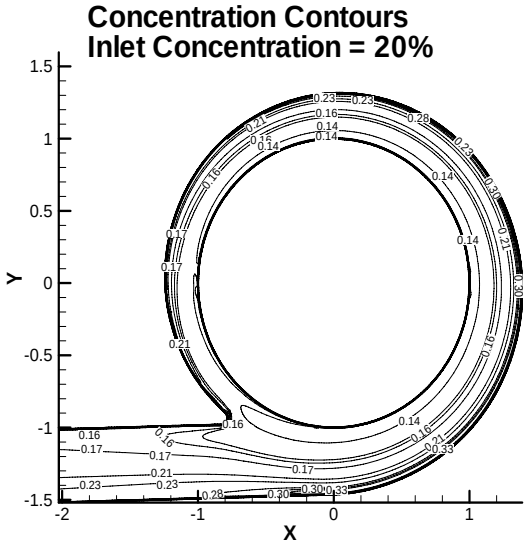

Fig. 10. Concentration contours inside the 2D domain of the pump casing (Casing No.3 in Table 1) for an average inlet concentration of 20% (by volume). Higher concentration along the casing wall is seen with peak value occurring in the belly region.

A. Effect of Inlet Solids Concentration

In Fig. 11, the effect on the solid concentration along the casing wall for various inlet solid concentrations is shown. Four particle concentrations at the inlet *viz.* 5%, 10%, 20% and 30% are considered. The particles are uniformly distributed around the casing inlet. In other words concentration at the inlet is averaged uniformly around the impeller exit periphery. The solid particles enter with equal velocity as of the carrier phase.

At every solid concentration, the peak value occurs at the point F and there exist a sharp discontinuity again at the tongue region. For an average concentration of 30% at inlet, the solid concentration along the casing wall varies from 11% to 36%. The difference in solid concentration between points A and G tends to be low for all the inlet concentrations. For example at 10% concentration, the concentration varies from 7% at point A to 15% at point G. This difference however becomes lesser for 20% and even lesser for 30% concentration.

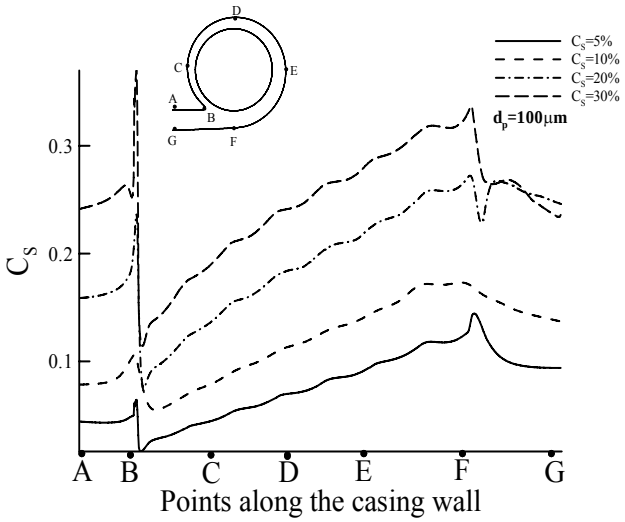

Fig. 11. Variations in solid concentration along the casing wall for different inlet concentrations *viz.* 5%, 10%, 20% and 30%.

The concentration along the casing wall increases monotonically from point B to point F. The peak position occurs somewhere near the point F and then it decreases. Concentration of solid phase does not vary much with flow rate variations (120% BEPQ, 100% BEPQ, 80% BEPQ and 60% BEPQ). This can be verified from Fig. 12. The trends of variations are same with the peak value observed in the belly region of the pump casing near the point F.

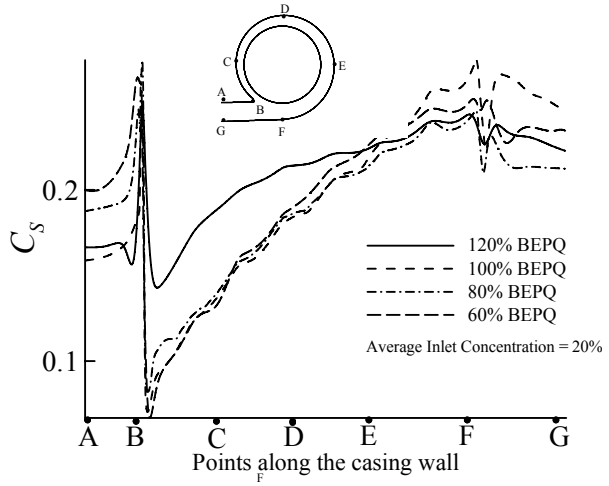

Fig. 12. Solid Concentration along the casing wall for various flow rates *viz.* 120% BEPQ, 100% BEPQ, 80% BEPQ and 60% BEPQ for an inlet particle concentration (C_S) of 20%.

B. Effect of Flow Rates

The pattern of solids velocity variations along the wall with varying flow rates requires special attention (see Fig. 13). In Fig. 13, the velocity profiles along the casing wall for various flow rates are shown. Non-uniform pattern of tangential velocity exists along the casing wall. The amount of variation are significant for 120% BEPQ and 60% BEPQ when compared to 100% BEPQ and 80% BEPQ. For higher flow rates *viz.* 120% BEPQ, an increase in the tangential velocity from point B to F is observed, as seen in Fig. 13. Whereas for the lower flow rates, opposite trends of tangential velocity variations are seen as it starts decreasing or remains uniform from point B to G. The pattern of the solid tangential velocity described here will bear serious implications on distribution of wall shear stresses along the casing wall.

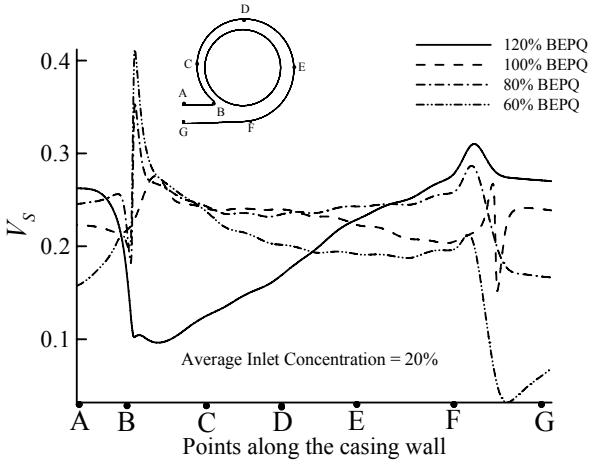

Fig. 13. Solid velocities along the casing wall for various flow rates *viz.* 60% BEPQ, 80% BEPQ, 100% BEPQ and 120% BEPQ for Casing No. 3 of Table 1. Note an inlet 20% particle concentration has been considered with a particle diameter of 100μm and density of 2650 kg/m^3.

In Fig. 14, trends of solid shear stress for various flow rates are shown along the casing wall. These shear stress values are non-dimensionalized w.r.t. ρU_0^2. The shear stresses for higher flow rates bear larger magnitude and have more unevenness compared to smaller flow rates (particularly 80% BEPQ and 60% BEPQ) as seen in the figure.

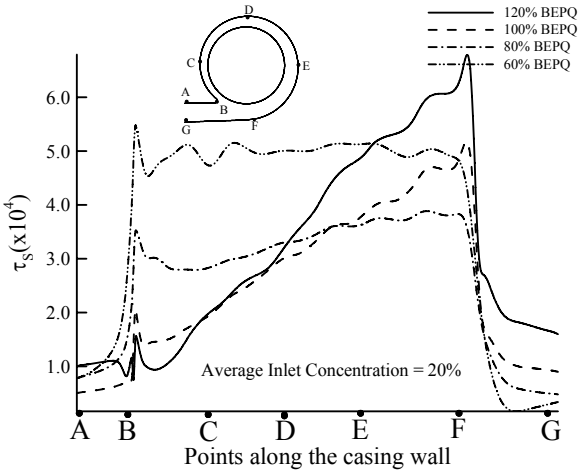

Fig. 14. Solid stresses along the casing wall for various flow rates *viz.* 60% BEPQ, 80% BEPQ, 100% BEPQ and 120% BEPQ for Casing No. 3 of Table 1. Note that an inlet particle concentration of

20% has been considered with a particle diameter of 100μm and density of 2650 kg/m^3.

C. Effect of Tongue Geometry

Solid stresses can be significantly affected by modifying the tongue geometry. The tongue geometry is modified in a manner by altering the OB to R ratio. Three different cases with an OB/R ratio equal to 1.2, 1.25 and 1.3 respectively are considered to study the effect on the shear stress distribution along the casing wall.

Fig. 15 shows the distribution of wall stresses along the casing wall for these three cases. As observed in the figure, with tongue drawn inwards with an OB/R ratio of 1.2, the peak wall shear stresses for the solid phase has been greatly reduced. The shear stress values are almost halved of the normal counterpart which is having an OB/R ratio of 1.25. With an OB/R=1.3 however, larger wall shear stresses are seen.

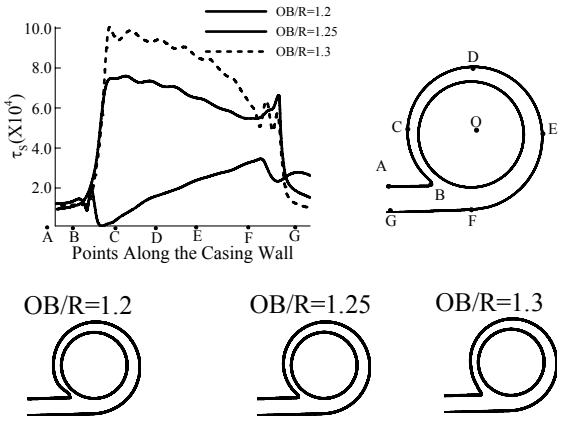

Fig. 15. Solid wall shear stress for different tongue geometries *viz.* OB/R =1.2, OB/R =1.25 and OB/R=1.3.

D. Effect of Casing Width

The effect of casing width on distribution of solid wall shear stresses is considered next. The casing width (b) appears in the inlet velocity calculations as following

$$u_\theta = \frac{gH}{\eta U_0} \quad and \quad u_r = \frac{Q}{2\pi R b}.$$

With an increase in the casing width, u_r decreases. The solid shear stress variations are seen in Fig. 16. With an increased width of the casing, lower shear stresses tend to exist along the casing wall with lesser unevenness. Five cases are shown with casing width being $b = 0.75b_0$, $b = 0.9b_0$, $b = b_0$, $b = 1.1b_0$ and $b = 1.25b_0$, respectively. The shear stresses for maximum casing width $b = 1.25b_0$ are minimum and less uneven as compared to lower casing widths. Casing width can have strong implications on the casing .

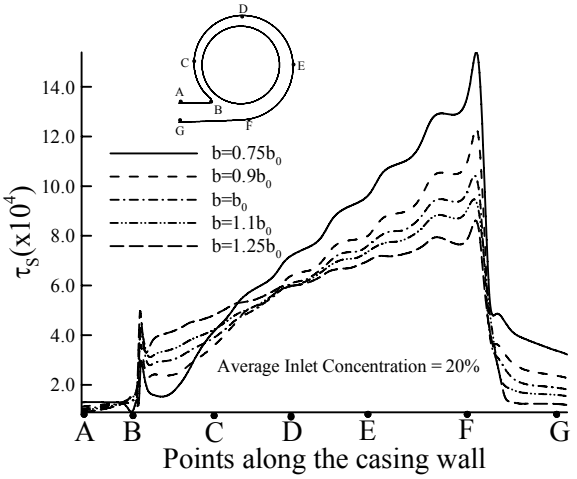

Fig. 16. Wall shear stress distribution along the casing wall for various casing widths *viz.* $b = 0.75b_0$, $b = 0.9b_0$, $b = b_0$, $b = 1.1b_0$ and $b = 1.25b_0$. These wall shear stresses for the solid phase are normalized w.r.t. ρU_0^2.

Operational conditions may also lead to reverse flow near the tongue region at some particular flow rate. In particular, reverse flow is expected at higher flow rates. Fig. 17 shows an enlarged view of the velocity vectors showing the reverse flow for the pump casing with diameter 502 mm (Ref. Casing No. 4 of Table 1). The tangential velocity and wall stresses are affected significantly near the tongue region due to this reverse flow.

Fig. 18 shows the tangential velocity along the casing wall which is showing an increase along the shell length. For normal flow (flow without reverse nature), the tangential velocity tends to remain uniform with a little rise along the length of the casing.

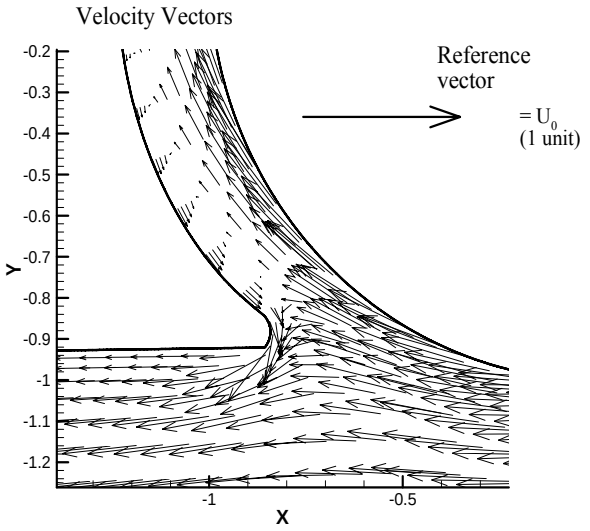

Fig. 17. Velocity vectors shown enlarged inside the pump casing near the tongue region. Note the recirculation near the tongue region of the pump (Casing No. 4 of Table 1).

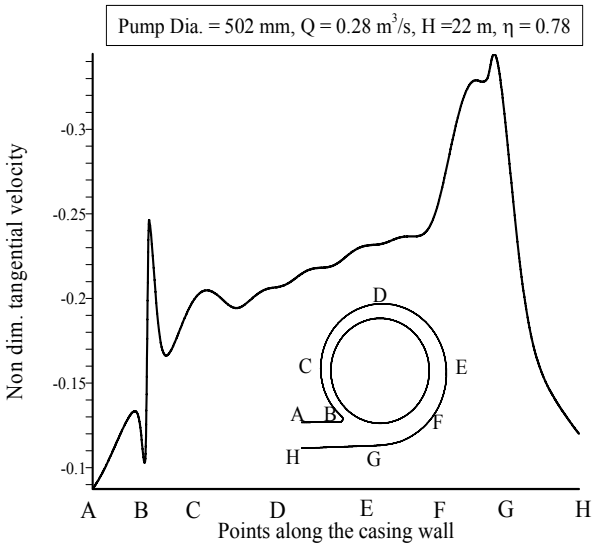

Fig. 18. Tangential velocity along the casing wall (Casing No. 4 of Table 1). The velocity is non-dimensionalized w.r.t. the impeller tip speed $(=U_0)$.

V. Conclusion

Dense slurry flow inside centrifugal pump casing using the Eulerian multiphase model in FLUENT 6.1® is presented. Mixture $k-\varepsilon$ turbulence model is used for modeling turbulence. The results of solids velocity and concentration distribution are verified against rigorous mesh independence. Validation of present predictions is carried out by comparing with experimental data and with published numerical results. Results in the case of pump casing are validated with FEM-based numerical results using mixing length model. Despite the difference in the turbulence models (k-ε Vs. mixing length), the results are found to be within 12% difference.

The effect of various operational and geometry conditions is considered on these quantities *viz.* wall shear stresses, solid concentration along the wall and tangential velocity along the wall. In particular effect of pump flow rate, tongue curvature, casing width, inlet concentration of the particles is considered on wall stress distribution and velocities along the wall.

Wall shear stresses are calculated and presented along with solid velocity and solid concentration along the casing wall. Solid concentration and solid wall shear stress increase monotonically from the upstream of the tongue region to the downstream of the belly region. These quantities are crucial in wear calculations along the casing wall.

Acknowledgment

The work is part of the research carried out at the Department of Applied Mechanics at Indian Institute of Technology Delhi, New Delhi, India.

References

[1] K.C. Wilson, G.R. Addie and R. Clift, *Slurry Transport Using Centrifugal Pumps*, Elsevier Science Publishers Ltd., Essex, England, 1992.

[2] A. Sellgren and L. Vappling, Effects of Highly Concentrated Slurries on the Performance of Centrifugal Pumps, Int. Symposium on Liquid-Solid Flows, New York, ASME-FED, Vol.38, 47pp. 143-148, eds. M.C. Roco, and W. Weidenroth, 1986.

[3] A. Sellgren, G.R. Addie, R Visintainer, K. V. Pagalthivarthi, Prediction of slurry pump component wear and cost, Proceedings, WEDA XXV and Texas A& M Annual Dredging Seminar, New Orleans, U.S.A., June 2005.

[4] G. R. Addie, A. Sellgren, J. Mudge, SAG mill pumping cost considerations. SAG Conference, *3rd International Conference on Autogenous & Semiautogenous Grinding Technology*, September 30 – October 3, 2001, Vancouver, B.C., Canada, 2001.

[5] M.C. Roco, P. Nair, G.R. Addie, Dennis J., "Erosion of Concentrated Slurry in Turbulent Flow," *ASME FED*, Vol. 13, pp. 69-77.

[6] Roco M C and Cader T (1988), Numerical method to predict wear distribution in slurry pipelines. Advances in Pipe Protection. BHRA Fluid Eng., Cranfield, UK, pp 53-85, 1984.

[7] K.V. Pagalthivarthi and F.W. Helmly, Applications of Materials Wear Testing to Solids Transport *via* Centrifugal Slurry Pumps, *Wear Testing of Advanced Materials*, ASTM STP 1167, eds. Divakar, R. and Blau, P.J., pp. 114-126, 1992.

[8] H.H. Tian, G.R. Addie, K.V. Pagalthivarthi, "Determination of wear coefficients for prediction through Coriolis wear testing", *WEAR*, Vol. 259, pp. 160-170, 2005.

[9] M.C. Roco and G.R. Addie, "Analytical Model and Experimental studies on Slurry flow and erosion in pump casings," *Slurry transportation*, STA, Vol.8, pp.263, 1983.

[10] K. V. Pagalthivarthi and G. R. Addie, "Prediction methodology for two-phase flow and erosion wear in slurry impellers", *4th International Conference on Multiphase Flow*, ICMF-2001, New Orleans, LA, May 27-June 1, 2001.

[11] G.R Addie and K.V. Pagalthivarthi, "Prediction of Dredge pump shell wear," *Proc. WODCON XII, 12th world dredging conference*, pp. 481-504, 1989.

[12] Roco, M.C., Addie, G.R. and Visintainer, R.J., 1985, "Study of Casing Performances in Centrifugal Slurry Pumps," *Particulate Science and Technology*, No.3, pp. 65-88.

[13] Pagalthivarthi, K.V., Desai, P.V. and Addie, G.R., 1990, "Particulate Motion and Concentration fields in Centrifugal Pumps," *Particulate Science and Technology*, No.8, pp. 77-96.

[14] G.R. Addie, K.V. Pagalthivarthi, J.R. Kadambi, "PIV and finite element comparisons of particles inside a slurry pump casing," *Proc. Int. Conf. on Hydrotransport* 16, Santiago, Chile, pp. 547-559, 2004.

[15] P. Charoenngam, A. Subramanian, J. R. Kadambi, G. R. Addie, "Investigations of slurry flow in a centrifugal pump using particle image velocimetry," 4th International conference on multiphase flow, New Orleans, May 27-June 1, 2001.

[16] M. Asuaje, F. Bakir, S. Kouidri, F. Kenyery, R. Rey, Numerical modelization of the flow in centrifugal pump: volute influence in velocity and pressure fields, International journal of rotating machinery, Vol. 3, pp. 244-255, 2005.

[17] M.E. Blanco, F.J. Fernandez, G. Parrondo, L. Jorge, .C. Santoria, "Numerical Simulation of Centrifugal Pumps," *Proc. Of ASME 2000 Fluids Engineering Division Summer Meeting*, Paper No. FEDSM200-11162, 2000.

[18] P. K. Gupta and K. V. Pagalthivarthi, Multi-size Particulate Flow through Rotating Channel – Modeling and Validation using Three Turbulence Models," International Journal of Computational Multiphase Flows, Vol. 1, No.2, pp. 133-160, 2009.

[19] P.K. Gupta and K.V. Pagalthivarthi, "Finite Element Modelling and Validation of Multi-size Particulate Flow through Rotating Channel," Progress in Computational Fluid Dynamics, Vol. 7, No. 5, pp. 293-306, 2007.

[20] K.V. Pagalthivarthi, J.S. Ravichandra, S. Sanghi, "Multi-size Particulate Flow in Horizontal Ducts: Modelling and Validation," Progress in Computational Fluid Dynamics, Vol. 5, Issue 8, pp. 466-481, 2005.

[21] A. Sellgren and G.R. Addie, "Cost-Effective Pumping of Coarse Mineral Products using Fine Sands," Powder Technology, Vol. 94, pp. 191-194, 1997.
[22] D.R. Kaushal and Y. Tomito, "Comparative Study of Pressure Drop in Multisized Particulate Slurry Flow through Pipe and Rectangular Duct," International Journal of Multiphase Flow, Vol. 29, No. 10, pp. 1473-1487, 2003.
[23] V.R. Ramanathan, "Prediction of Two-Phase Free Surface Flow in Rotating Channels," Doctoral dissertation, Indian Institute of Technology, New Delhi, 2001.
[24] C.-Y. Wen and Y. H. Yu. Mechanics of Fluidization.Chem. Eng. Prog. Symp. Series, 62:100-111, 1966.